ACS OMEGA

http://pubs.acs.org/journal/acsodf

Article

Covalent Conjugation of Carbon Dots with Plasmid and DNA Condensation Thereafter: Realistic Insights into the Condensate Morphology, Energetics, and Photophysics

Suman Nayak and Prolay Das*

Cite This: *ACS Omega* 2021, 6, 21425−21435

Read Online

ACCESS | Metrics & More | Article Recommendations | Supporting Information

ABSTRACT: The use of carbon quantum dots (CDs) as trackable nanocarriers for plasmid and gene as hybrid DNA condensates has gained momentum, as evident from the significant recent research efforts. However, the in-depth morphology of the condensates, the energetics of the condensation process, and the photophysical aspects of the CD are not well understood and often disregarded. Herein, for the first time, we covalently attached linearized pUC19 with citric acid and cysteamine-derived CD through the reaction of the surface amine groups of CDs with the 5′-phospho-methyl imidazolide derivative of the plasmid to obtain a 1:1 CD-pUC19 covalent conjugate. The CD-pUC19 conjugates were further transformed into DNA condensates with spermine that displayed a toroidal morphology with a diameter of ∼200 nm involving ∼2−5 CD-pUC19 conjugates in a single condensate. While the interaction of pristine CD to spermine was exothermic, the binding of the CD-pUC19 conjugate with spermine was endothermic and primarily entropy-driven. The condensed plasmid displayed severe conformational stress and deviation from the B-form due to the compact packing of the DNA but better transfection ability than the pristine CD. The CDs in the condensates tend to come close to each other at the core that results in their shielding from excitation. However, this does not prevent them from emanating reactive oxygen species on visible light exposure that compromises the decondensation process and cell viability at higher exposure times, calling for utmost caution in establishing them as nonviral transfecting agents universally.

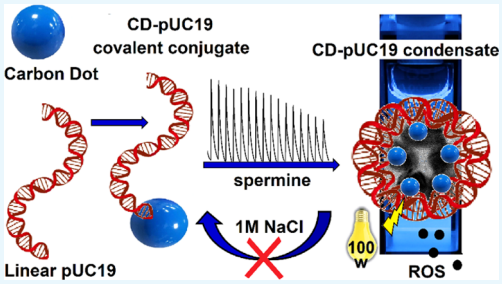

INTRODUCTION

The intrinsic photoluminescence (PL), tunable surface properties, ease of synthesis, and reasonably high shelf life of carbon dots (CDs) have prompted researchers to explore them in imaging, optoelectronics, biosensing, drug delivery, and theranostic applications.[1−3] Few recent research studies have also hinted toward the dual use of CDs in optogenetics, where CDs act as a carrier of plasmid DNA encoding a gene and a fluorescence tracker in transfection.[4−10] CDs with surface positive charge wrap negatively charged DNA of interest into condensates,[11] similar to other nanoparticles without using traditionally used multivalent cations such as spermine, spermidine, and Co(III) salts.[12,13] However, the exact nature of such a DNA condensation process on CDs is seldom addressed and poorly understood. Contextually, the interaction between the CD and DNA in all these studies is purely electrostatic that poses many unanswered questions than resolved.

While electron microscopy images in few instances confirmed the formation of condensates,[4−7] there is no guarantee that throughout the transfection process, the electrostatically attached DNA is retained and remains intact with the CD that involves its transport across the cell membrane and sometimes the nuclear membrane. Tracking of the CD through fluorescence-based imaging is often displayed to substantiate the claim of internalization of the CD−DNA condensates into cells. Occasionally, this could be error-prone since such imaging is based on the CDs' excitation/emission and not the DNA whose presence on the CD surface cannot be confirmed at that instant by any means. In this perspective, covalent conjugation of the DNA to CD may be beneficial where the fluorescence output could be directly equated to the amount of DNA cargo delivered in the cell. However, given the huge number of nucleobases in plasmids in the range of 2.5−3.5 kbp and related steric hindrances, coupled with the low reactivity of the terminal phosphates, covalent conjugation of plasmid DNA with CD and other nanoparticles is a formidable proposition that is seldom addressed. Herein, for the first time, we report the successful chemical conjugation of a linearized pUC19 plasmid DNA with CD to achieve the CD-pUC19 covalent conjugate

Received: April 28, 2021
Accepted: August 5, 2021
Published: August 13, 2021

Scheme 1. Synthesis of the CD-pUC19 Covalent Conjugate and Subsequent Condensate Formation

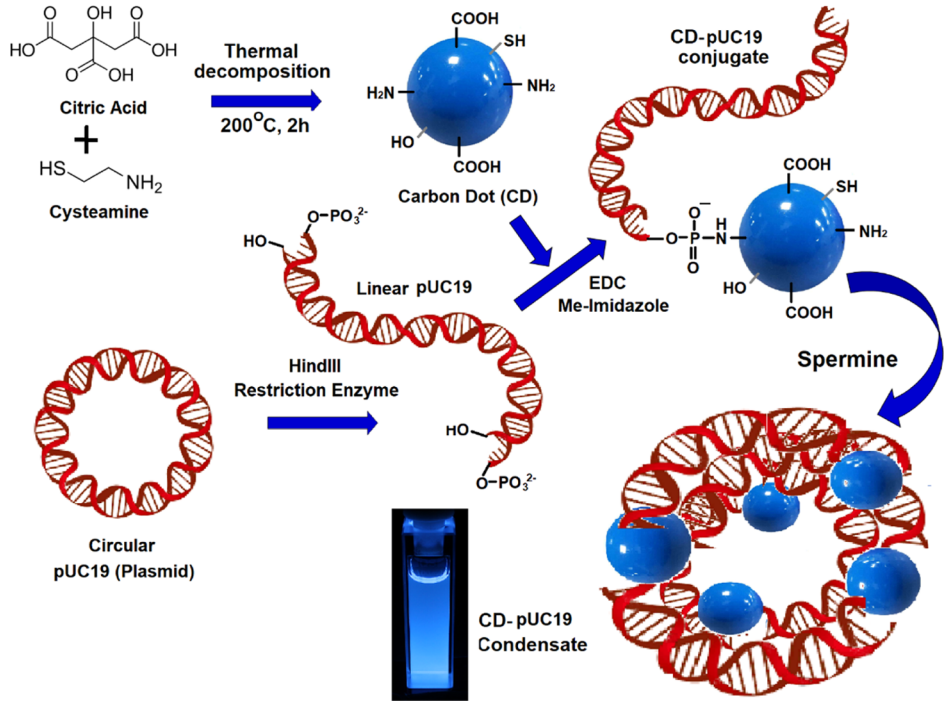

that is subsequently transformed into condensates, employing spermine as a condensing agent.

Furthermore, some relevant questions may be asked by the research community for which we are yet to get definite answers. Do we know how many plasmid DNAs or CDs are actually present in a single condensate, the thermodynamics that guides the condensation process, or the comparative fluorescence output of the CD before and after condensation? These issues gain relevance and prompt further investigation to evaluate the feasibility of the CD−DNA condensates envisioned as potential transfection agents, which we have tried to address in the present study.

Reportedly, plasmid DNA condensed with the cationic CD synthesized from arginine-glucose and hyaluronic acid demonstrated gene delivery with simultaneous fluorescence tracking.[5,10] Elsewhere, polymeric CDs (pCDs) have been used to achieve DNA condensation with plasmid DNA.[4,7,8,14,15] CDs coated with cationic polymers such as polyethyleneimine (PEI) have also been used to achieve the condensation of plasmid DNA.[16] Plasmid DNA condensates were also created using a polysaccharide-derived CD for faster mesenchymal stem cell differentiation.[17] However, all the previous studies mentioned above do not involve covalent conjugation of the plasmid cargo with the CD or pCD, making it difficult to comment on the composition of the DNA condensates with surety. Moreover, the pioneering work by Victor Bloomfield had reported the thermodynamics of the DNA condensation process, the understanding of which is important in the context of the co-condensation of DNA with CD, which is often ignored.[12,18,19] Additionally, to the best of our knowledge, none of the CDs involved in DNA condensation reported so far meant for gene transfection applications have been evaluated for reactive oxygen species (ROS) generation on photon excitation, including natural light. This is a highly probable photophysical aspect of the CD other than fluorescence.[20−22] The ROS generation ability of the CD essentially requires additional measures for storage and relevant toxicity evaluation to determine its suitability for in vivo applications. Unfortunately, toxicity studies done so far applicable to CD−DNA condensates only partially account for the CDs' concentration.

The possibility of creating novel CDs and using them with DNA to form condensates for optogenetic applications calls for revisiting the basic principles of DNA condensation and properties of the CD in the inclusive purview of CD. Toward this, we present the optimization of reaction conditions between the terminal phosphate groups of the linearized pUC19 plasmid and $-NH_2$ (amino) groups on the surface of the CD to achieve covalent conjugation between CD and pUC19. Transformation of the CD-pUC19 into condensates provided us the much-needed appraisal of the condensate morphology through electron microscopy, quantitative thermodynamic parameters of the condensation through calorimetric measurements, and photophysical implications, including ROS generation from the CD with steady-state and time-resolved studies. The condensation process of the CD-pUC19 conjugate was carefully evaluated to understand the morphology of the resulting condensates, the thermodynamics of the condensation process, and the comparative efficiency of the fluorescence of CD before and after condensation (Scheme 1).

RESULTS AND DISCUSSION

Synthesis and Characterization of CDs. CDs were synthesized by the thermal decomposition method with citric acid and cysteamine as substrates in water, the latter being the source of N and S dopants.[21−23] The CD solution was purified by centrifugation to remove larger aggregates and dialysis to remove smaller undesirable fluorophores and starting materials. The CD revealed a semispherical morphology with an average diameter of ∼15 nm through atomic force microscopy (AFM) and transmission electron microscopy (TEM) analysis (Figure 1A,B). The energy-dispersive spectrometry (EDS)

https://doi.org/10.1021/acsomega.1c02247
ACS Omega 2021, 6, 21425−21435

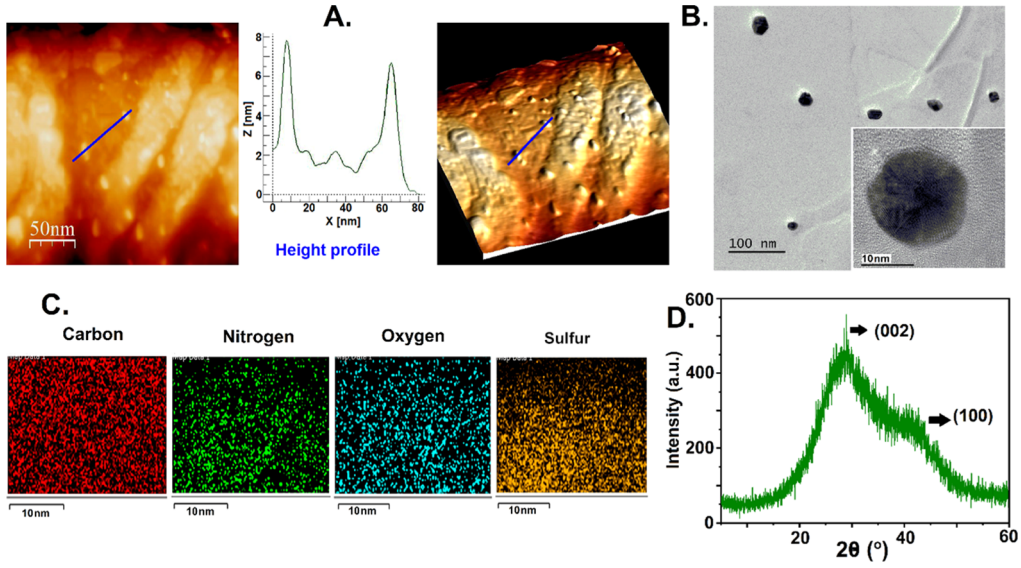

Figure 1. Characterization of CDs. (A) AFM image of CDs with the height profile. (B) TEM image of CDs (inset, single CD). (C) Elemental mapping of CDs showing the presence of C, O, N, and S. (D) PXRD pattern of CDs showing peaks for 002 and 100 planes.

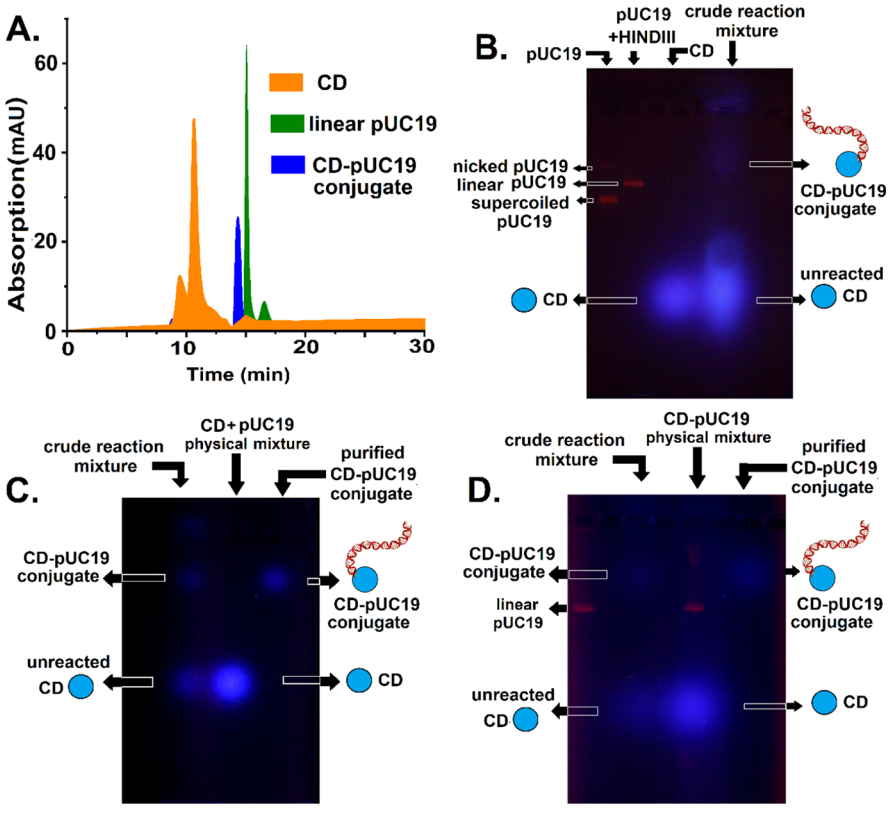

Figure 2. Characterization of the CD-pUC19 conjugate. (A) RP-HPLC analysis of CD, linear pUC19, and CD-pUC19 conjugate. (B) Agarose gel electrophoresis of pUC19, CD, and crude reaction mixture. (C) Agarose gel electrophoresis before EtBr staining of crude and purified CD-pUC19 conjugate and physical mixture of CD and linear pUC19. (D) Same gel as (C) after EtBr staining.

analysis of the CD confirmed the presence of carbon (C), nitrogen (N), oxygen (O), and sulfur (S) (Figures 1C and S1, Supporting Information). The high-resolution TEM (HRTEM) image of the CD (Figure S2, Supporting Information) showed an identical and well-resolved lattice with a spacing of ~0.25 nm, indicating the presence of the (100) facet of sp^2 graphitic carbon. The crystalline character of the CD was further recognized by powder X-ray diffraction (PXRD) analysis (Figure 1D), where a sharp diffraction peak at ~28.6° and a very weak peak at ~41.2° were observed corresponding to (002) and (100) planes, respectively.[24] The peak at ~28.6° represents the characteristic interplanar stacking of aromatic systems of the graphitic structure. The slightly upward shift (from 26.5 to 28.6°) compared to the ordered crystal structure of graphite points to the presence of disordered carbon and a reduction in the spacing of the sp^2

https://doi.org/10.1021/acsomega.1c02247
ACS Omega 2021, 6, 21425−21435

layers during the carbonization process. The low-intensity peak at ∼41° points toward the significant presence of amorphous carbon in the CD, which is well correlated with the results obtained from the selected area electron diffraction (SAED) pattern (Figure S3, Supporting Information).[20]

The surface functional groups present on the CD were determined by Fourier transform-infrared spectroscopy (FT-IR), where peaks for C═O stretching (1730 cm^{-1}), N−H, O−H, C−H stretching (broad, 2700−3600 cm^{-1}), C−H bending (1327 cm^{-1}), O−H bending (1412 cm^{-1}), and C−O bending (1136 cm^{-1}) were observed, confirming the presence of −COOH, −OH, and $-NH_2$ groups (Figure S4, Supporting Information).[21,22] Using UV−vis spectroscopy (Figure S5, Supporting Information), a peak at 350 nm wavelength (λ_{max}) corresponding to the $n-\pi^*$ transition of lone pair of electrons present on the −COOH and $-NH_2$ groups was observed. The excitation-independent fluorescence emission of CD was demonstrated from steady-state fluorescence emission spectra (Figure S6, Supporting Information) that showed strong emission of the CD at 425 nm when excited in the wavelength range of 330−360 nm with the strongest emission at 345 nm excitation. The fluorescence quantum yield of the CD was found to be ∼43% with respect to quinine sulfate (QY = 0.55) in 0.5 M H_2SO_4 as standard.

Synthesis and Characterization of the CD-pUC19 Covalent Conjugate. pUC19 was treated with HINDIII restriction endonuclease to linearize the plasmid. The reaction between the terminal 5′phosphate ends of the linearized pUC19 and the $-NH_2$ groups on the surface of the CD was optimized to create the CD-pUC19 conjugate. Our effort to covalently conjugate pUC19 with an in-house-developed branched PEI-based CD (BPEI, data not shown) was unsuccessful, possibly due to the strong electrostatic interaction between the DNA and the CD that restricts favorable collisional effects for the phosphoramidation reaction to occur. Methyl imidazole was found to be more effective in activating the terminal phosphates of pUC19 in the presence of 1-(3-dimethylaminopropyl)-3-ethylcarbodiimide (EDC) than imidazole. Also, the reaction yield was appropriate for further downstream applications only when CD was used in huge excess, which is understandable given the size and steric considerations of pUC19. The success of the conjugation was confirmed by reverse-phase HPLC (RP-HPLC) analysis, where the retention time of CD-pUC19 was found to be distinctly different and between linear pUC19 and pure CD (Figure 2A). Furthermore, we employed agarose gel electrophoresis to ascertain the electrophoretic mobility of the CD-pUC19 conjugate. The crude reaction mixture showed the presence of unreacted CD with the emergence of a new band having restricted mobility than pure CD and distinctly different from supercoiled, linear, or open circular pUC19 (Figure 2B). Dialysis of the crude reaction mixture eliminated unreacted CD and reaction debris effectively, as visualized from the absence of the CD band and clean well in the gel for the purified CD-pUC19 conjugate (Figure 2C). To check the presence of unreacted pUC19 in the reaction mixture, we stained the same agarose gel with EtBr after visualization and recording of the image without EtBr staining (Figure 2D). Although the emergence of EtBr-stained linear pUC19 control was clearly visible in the gel, no band for linear pUC19 was found in the purified reaction mixture under the optimized reaction conditions. The appearance of the linear pUC19 band in the physical mixture of CD and pUC19 shows the independent movement of each component without any significant co-dragging. We compared the mobility of the CD-pUC19 conjugate with 1 kbp plasmid ladder that appears between 4 and 5 kbp. In all possibility, the conjugation reaction is restricted to the covalent attachment of one plasmid with one CD due to the moderate reactivity of the terminal phosphates and significant steric factor introduced by the plasmid in the reaction (Figure S7, Supporting Information). Nevertheless, the covalent conjugation between a plasmid and CD has been demonstrated here beyond reasonable doubt that is achieved for the very first time.

DNA Condensation with the CD-pUC19 Conjugate. It is now well known that the treatment of polycations such as spermine and spermidine with DNA neutralizes the negative charge of the DNA backbone and leads to the formation of DNA condensates.[12,25,26] In this study, we did not use any cationic CD, so condensation of the CD-pUC19 conjugate was achieved through titrating the conjugate sample with a calculated amount of spermine. Agarose gel electrophoresis performed with the CD-pUC19 conjugate solution showed heavy dragging of the band upon addition of 25 μM spermine that virtually ceases to move in the gel matrix with a further increase of spermine concentration to 50−100 μM (Figure 3A). This indicates that the condensation of the CD-pUC19 conjugate was partial and incomplete at a lower spermine concentration and was accomplished at a higher concentration of 50 μM or beyond where the band corresponding to the CD-pUC19 conjugate was completely absent. A close look at the agarose gel also reveals a slight movement of CD-pUC19 in the opposite direction toward the anode with the addition of 100 μM spermine that points to the complete charge neutralization and subsequent charge reversal of the CD-pUC19 entity under such conditions.

The electrokinetic potential and hence the surface charge of the CD were obtained as +14.6 mV, which decreased to +7.4 mV upon conjugation of CD with the plasmid in the CD-pUC19 conjugate (Figures 3B and S8, Supporting Information). As expected, the negative charge of the plasmid (−26.1 mV) is held responsible for lowering the zeta potential of CD after its conjugation.[5] However, the zeta potential of the CD-pUC19 conjugate increased to ∼+25 mV after the addition of 100 μM spermine that points to the formation of the CD-pUC19 condensate. The results of zeta potential measurements positively correlate with dynamic light scattering (DLS) experiments where the light scattering intensity and the average hydrodynamic radii of the CD-pUC19 conjugate steadily increased with the addition of spermine in the titration mode (Figure 3C).[27] At 50 μM spermine concentration, a broad size distribution (30−150 nm) was obtained, having an average hydrodynamic diameter of ∼90 nm (Figure S9, Supporting Information). However, with the increase in spermine concentration to 100 μM, the light scattering intensity increased, and sharp size distribution was obtained, indicating the formation of stable CD-pUC19 condensates having an average hydrodynamic diameter of ∼300 nm (Figure 3C). With a further increase in spermine concentration to 200 μM or more, an abrupt increase in intensity and radii was found, indicative of the formation of aggregates that eventually precipitate from the solution (Figure S10, Supporting Information).

The CD-pUC19 condensates achieved through the addition of 100 μM spermine were directly visualized with TEM and AFM imaging (Figure 4A,B). We observed well-dispersed CD-

https://doi.org/10.1021/acsomega.1c02247
ACS Omega 2021, 6, 21425−21435

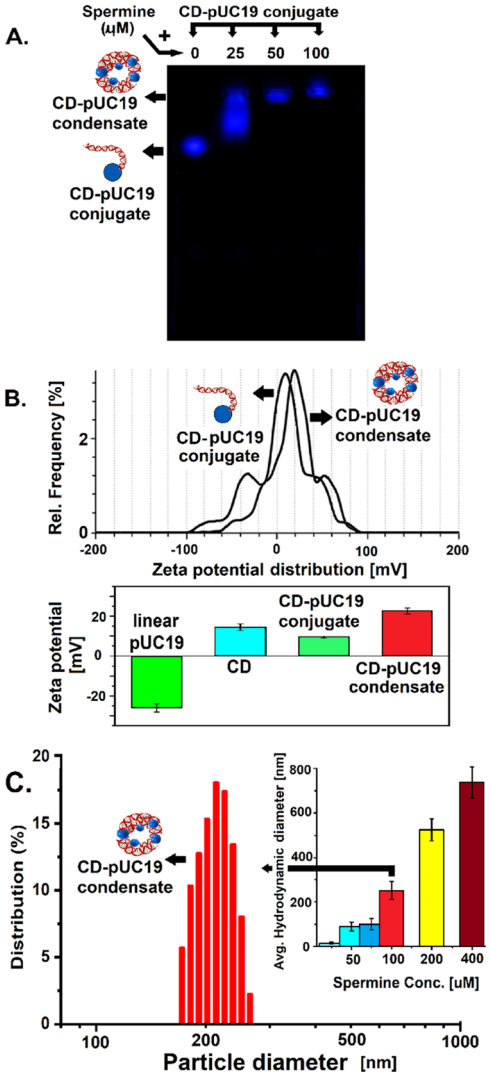

Figure 3. (A) Agarose gel electrophoresis showing the mobility of the CD-pUC19 conjugate in the presence of spermine. (B) Zeta potential of CD, pUC19, CD-pUC19 conjugate, and its condensate. (C) DLS spectra of CD-pUC19 condensation in the presence of different concentrations of spermine and their size distribution. Error bar represents standard deviation from the average of three acquisitions of separate samples done on three different days.

pUC19 condensates mostly having a toroidal morphology with a diameter of ∼200 nm and embedded fine knots in AFM. The cross-sectional analysis of the CD-pUC19 condensate shows significantly lower height at the center portion of the condensate that further upheld the toroidal morphology.[28] An interesting observation from TEM imaging (without any staining) was that CD was found to have the tendency to be placed close to each other, possibly due to the electrostatic interaction owing to their zwitterionic nature. Contrary to the common notion that a single CD is involved with a single plasmid in CD-pUC19 condensates, our study shows that the condensation of plasmid DNA on CD involves multiple CD and plasmid entities where CD tends to get closer to each other. The present study successfully shows the involvement of ∼2−5 CDs and hence an equal number of plasmids in individual CD-pUC19 condensates, which is commonly overlooked with negative staining in TEM.

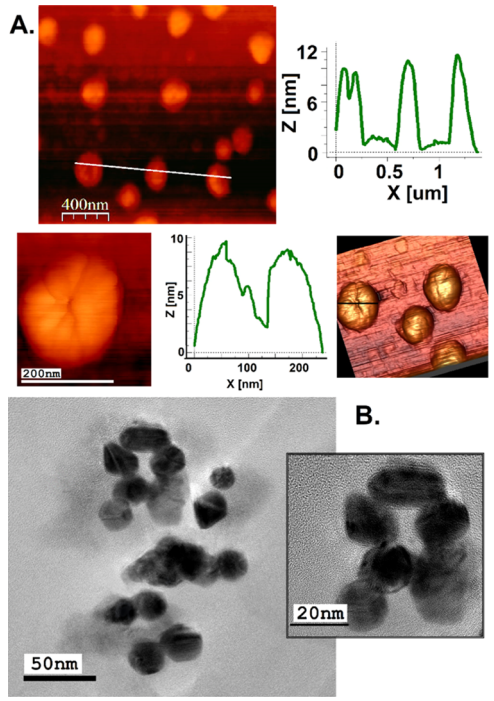

Figure 4. (A) AFM image and height distribution. Samples are drop-cast on mica sheets for imaging. (B) TEM image of CD-pUC19 condensates in the presence of 100 μM spermine. Samples are drop-cast and air-dried on carbon-coated copper grids.

To check the dependency of processing conditions on the number of CD-pUC19 conjugates present in CD-pUC19 condensates during the formation of the assembly, we increased the temperature from 25 to 40 °C, increased the ionic strength from 10 to 50 mM sodium phosphate buffer, and increased the pH from 7.2 to 9, keeping the spermine concentration unchanged (100 μM). In all three conditions, we found multiple CD-pUC19 conjugates associated with a single condensate (Figure S11, Supporting Information). However, DLS analysis showed a reduction of hydrodynamic radii in all three cases, indicating more compaction due to the change in assembly conditions. Thus, irrespective of the increase in temperature, ionic strength, and pH, we failed to achieve condensates made out of a single CD-pUC19 linear conjugate.

Thermodynamics of CD-pUC19 Condensation and Photophysical Studies. Isothermal titration calorimetry (ITC) was employed to examine the binding ability of pUC19, CD, and CD-pUC19 with spermine (Figure S12, Supporting Information). Representative binding isotherm of pUC19 interaction with spermine fitted to a single-site binding model showed an overall endothermic heat of reaction (ΔH = 15.1 kcal/mol; Table S1, Supporting Information), and the predominant positive entropy ($T\Delta S$ = 20.99 kcal/mol) indicates that the binding was driven by Groove binding, as reported in the literature.[29,30] However, ITC profiles for CD binding with spermine showed that the reaction is exothermic in nature, resulting in spontaneous interaction due to the negative value of Gibbs free energy (G). The negative value of both enthalpy change (ΔH = −8.46 kcal/mol) and entropy change ($T\Delta S$ = −1.68 kcal/mol) indicated a major role of van der Waal's interactions and hydrogen bond formation between the surface functional groups of CD and positive charge of spermine. The binding of the CD-pUC19 conjugate with

https://doi.org/10.1021/acsomega.1c02247
ACS Omega 2021, 6, 21425−21435

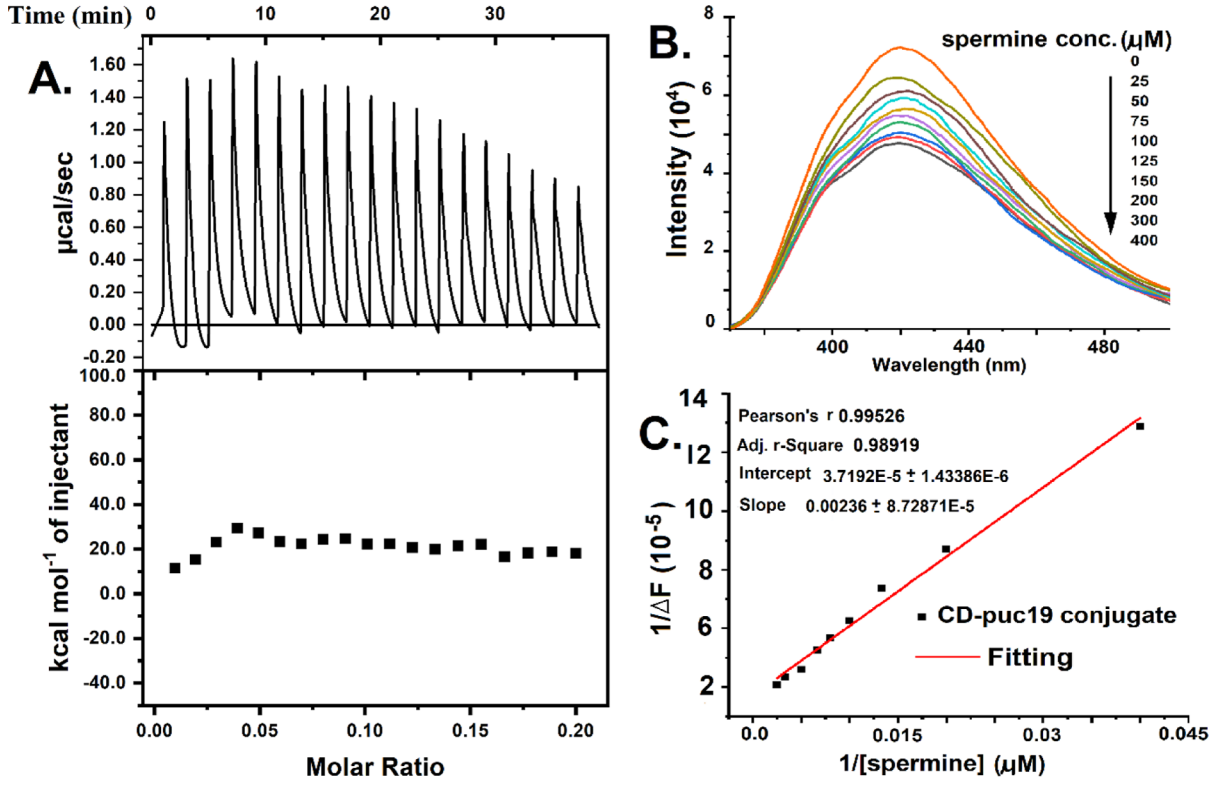

Figure 5. (A) ITC profile of the CD-pUC19 conjugate with spermine fitted to a single-site binding model. (B) Fluorescence titration of the CD-pUC19 conjugate with the increasing concentration of spermine. (C) Benesi−Hilderbrand plot of the CD-pUC19 conjugate and spermine.

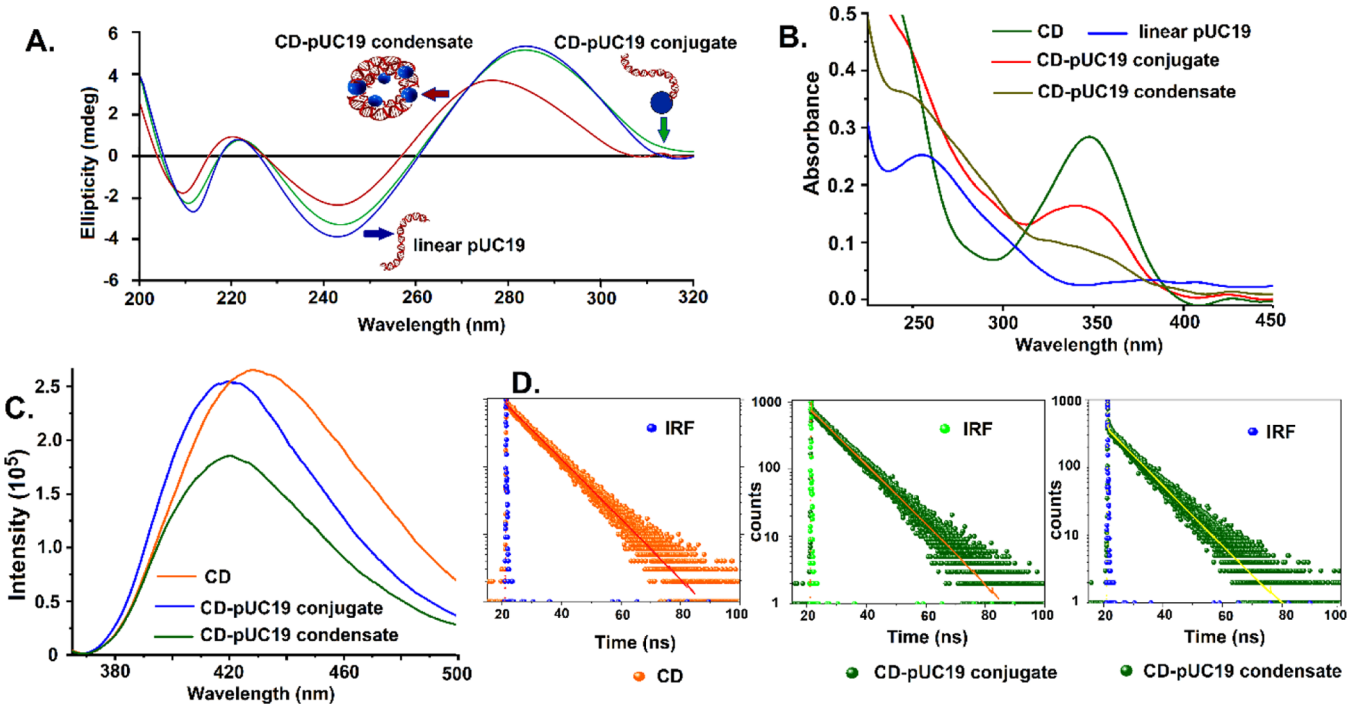

Figure 6. (A) Circular dichroism spectra. (B) UV−vis spectra. (C) Steady-state spectra. (D) Fluorescence lifetime decay of CD, CD-pUC19 conjugate, and CD-pUC19 condensate.

spermine (Figure 5A) was found to be endothermic in nature with higher unfavorable ΔH (22.5 kcal/mol). Thus, the observed binding was favored by significant entropy ($T\Delta S^\circ$ = 30.3 kcal/mol) contribution driven by the release of structured water molecules surrounding the binding surfaces of CD-pUC19 conjugates, suggestive of the dominance of solvation entropy over conformational entropy.[29−31] In terms of thermodynamics, positive ΔH° usually indicates that the complex formation between CD-pUC19 and spermine is mainly driven by the hydrophobic interaction through DNA

https://doi.org/10.1021/acsomega.1c02247
ACS Omega 2021, 6, 21425−21435

grooves. Nevertheless, the negative standard Gibbs energy ($\Delta G°$) value of the binding of pUC19, CD, and CD-pUC19 conjugate with spermine is attributed to the thermodynamically favorable binding between them. Although the greater value of equilibrium association constant (4.47×10^5 M^{-1}) suggests a stronger association of the CD-pUC19 conjugate to spermine than the binding of the only CD to spermine (7.71×10^4), the latter phenomenon is responsible for the enhanced concentration of spermine required to achieve complete condensation than normally required.[32]

We also evaluated the interaction of the CD and CD-pUC19 conjugate with different spermine concentrations (25−400 μM) based on the PL of the CD by carrying out fluorescence titration. The fluorescence intensity of the CD remains unchanged with the addition of spermine (Figure S13, Supporting Information). However, the CD-pUC19 conjugate showed a gradual weakening of fluorescence intensity with the increasing concentration of the spermine, one reason being the placement of the CD into the core of the condensate (Figure 5B). To unveil the strength of the interaction between the CD-pUC19 conjugate and spermine, association constant values were calculated from the fluorescence measurements using the Benesi−Hildebrand plot (Figure 5C).[29] This confirms stronger interaction of the CD-pUC19 conjugate ($K_b = 1.6 \times 10^4$ M^{-1}) with spermine compared to only CD ($K_b = 4.13 \times 10^3$ M^{-1}), evidently suggesting a pronounced binding affinity of the spermine to the CD-pUC19 conjugate.

The conformational changes of the DNA brought about by the condensation process were ascertained by circular dichroism spectroscopy (Figure 6A). The circular dichroism spectrum of the linear plasmid showed a positive band at 280 nm due to base stacking and a negative band at 245 nm due to the helicity characteristic of right-handed B-form DNA that remains virtually unchanged after its conjugation with CD, confirming the retention of the B-form of plasmid after covalent conjugation. In the presence of spermine, the positive band at 280 nm is significantly blue-shifted (~10 nm) with a loss of intensity for both the positive and the negative peaks. This suggests that the stacking mode and the orientation of base pairs in DNA were disturbed upon condensation, introducing a conformational change toward the A-form in the condensates.[33] Using UV−vis spectroscopy, the peak at 350 nm (λ_{max}) corresponding to the $n-\pi^*$ electronic transition of the lone pair present on the functional groups of CD was observed (Figure 6B). The presence of the characteristic peak of DNA at ~260 nm in the CD-pUC19 conjugate along with the CD peak is an indirect confirmation of the covalent association of CD. However, with a similar concentration of CD in both CD-pUC19 conjugate and the corresponding condensate, the absorbance intensity was subdued in the latter. The comparative fluorescence emission of the CD, CD-pUC19 conjugate, and CD-pUC19 condensate at an excitation wavelength of 345 nm showed a negligible blue shift (~5 nm) of CD after plasmid conjugation due to few amine modifications on the surface of the CD (Figure 6C).[34] However, a significant loss of fluorescence intensity was observed after the transformation of the CD-pUC19 conjugate into condensates. This is purely a shielding effect where CDs are embedded inside the condensates and tend to be shielded from uniform excitation. The average fluorescence lifetime of the CD was estimated as ~9.87 ns that slightly decreased after condensate formation that correlates well with the blue shift in excitation, resulting from the slight loss of some amine functionality on the surface of the CD due to conjugation (Figure 6D and Table S2, Supporting Information).[36]

ROS Generation Study and Transfection Efficiency. Previous research has shown that many CDs are adept at ROS generation on irradiation by normal light in the visible region.[20−22] This prompted us to irradiate the CD and CD-pUC19 condensates with visible light from a tungsten source (100 W, 30 cm distance) and evaluate any possible ROS generation using nonfluorescent dihydrorhodamine 123 (DHR 123) that is converted into fluorescent rhodamine 123 on exposure to ROS (Figure 7). Although the amount of ROS

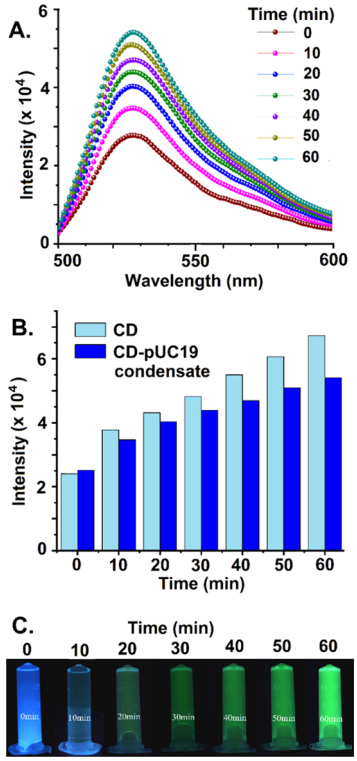

Figure 7. (A) Fluorescence spectra of ROS generation in the presence of DHR 123 by the CD-pUC19 condensate under the visible light (tungsten bulb, 100 W, 30 cm distance). (B) Comparison of the ROS generation efficiency of CD and CD-pUC19 condensate. (C) Digital images of ROS generation with the time of irradiation of the CD-pUC19 condensate after the addition of DHR 123.

generated from CD present in CD-pUC19 condensates was found to be consistently lower than pristine CD, the ROS generation ability of the CD is still significantly retained so as to be visually detectable with DHR 123 (Figure S14, Supporting Information). Surprisingly, we observed that the decondensation of CD-pUC19 condensates with 1 M NaCl was incomplete with the appearance of heavy smearing of the gel electrophoresis band, probably due to ROS-induced chemical alteration at some sites in the DNA (Figure S15, Supporting Information). This phenomenon should be considered with caution particularly during material handling and storage when researchers intend to develop gene delivery vectors based on CD. The possibility of damage to the nucleobases in the therapeutic gene by the ROS generated from the CD cannot be ignored that could bear devastating consequences. Additionally, we found reduced cell viability on irradiating the CD-pUC19 condensates up to 1 h of light exposure that confirms toxicity issues at the higher time of light

https://doi.org/10.1021/acsomega.1c02247
ACS Omega 2021, 6, 21425−21435

exposure irrespective of the synthetic methodology (hydrothermal or thermal decomposition) (Figure S16, Supporting Information).[21]

The less cytotoxicity, biocompatibility, extraordinary aqueous solubility, and inherent fluorescence properties of CDs make them valuable candidates as a probe to track transfection efficiency. The CD-pUC19 condensates were found to be more efficiently transfected in HEK293 cells than pristine CD, as determined from the fluorescence intensity of CD inside the cells through confocal imaging (Figure S17, Supporting Information). Given the residual positive charge on the condensate surface, a better transfection efficiency of CD-pUC19 condensate was obtained than the pristine CD.

The covalent conjugation between a linear plasmid and CD necessitated significant optimization efforts to drive the reaction forward owing to the huge size of the plasmid and the accompanied steric considerations, not to mention the low reactivity of the 5′phosphate terminals. The conjugation failed with cationic CD, stoichiometric use of the present CD, or using imidazole to create the 5′-phosphorimidazolide DNA. We have accomplished the said covalent conjugation through careful manipulation of the EDC-methyl imidazole-based phosphoramidation chemistry and varying substrate concentration. Characterization of the CD-pUC19 conjugation with gel electrophoresis and RP-HPLC hints toward a 1:1 conjugation between the 5′phosphate ends of a plasmid with the $-NH_2$ group of a CD. The CD-pUC19 conjugate was transformed into condensates by spermine and studied to determine its morphology and photophysical properties. The positive zeta potential of the CD was significantly reduced after its covalent conjugation with the plasmid, which increased again upon condensation, indicating charge neutralization on the DNA backbone. The condensates showed predominantly toroidal morphology, as evident from AFM studies. Significant deviation from B-conformation in the plasmid DNA was recorded that points to the compact packing and increase in hydrophobicity during the condensation. Interestingly, we found the involvement of multiple CD-pUC19 conjugates (approximately 2−5) in a single condensate where the CD tends to get in close packing toward the core of the condensates, resulting in shielding of the CD to reduce the efficiency of its absorption and emission. However, the fluorescence lifetime remains significantly unchanged, which is a concentration-independent photophysical aspect. The CD was found to generate ROS when exposed to normal visible light from a tungsten source that suppresses cell viability at higher exposure times that demand restraint in choosing the CD for potential transfection applications.

CONCLUSIONS

Recent research has enthusiastically projected CD as a nonviral vector for gene delivery applications. This concept stems from the wide range of substrate scope and the ease of synthesizing CD with a positive surface charge. The surface positive charge electrostatically binds the DNA and is being employed for gene delivery applications with the added advantages of monitoring the assembly through the intrinsic fluorescence of CD. However, the morphology of the CD-DNA condensates at the molecular level, the energetics of the condensation, conformational implications of the DNA, and the photophysics need more understanding. This knowledge is essential to establish CD as worthy of the research effort dedicated to the race of finding novel transfecting agents. This prompted us to covalently conjugate a linear pUC19 plasmid DNA with CD to hypothesize that under any circumstances, the DNA and the CD are intact in circulation and during the transfection process, and also, the observed photophysics of the CD is resultant of its attachment with DNA. Apart from achieving the covalent conjugation of a plasmid with CD, for the first time, we evaluated the thermodynamic parameters of binding of spermine with the CD-pUC19 conjugate that proved the significant contribution of entropy in driving the condensation forward. Our studies also showed that multiple pUC19 conjugates are involved in a single condensate where the DNA in the condensate deviates considerably from the traditional B-form with ∼2−5 CDs closely placed to each other in a single condensate with a remote possibility of obtaining absolute uniformity. Such insights are not being revealed from previous research and definitely add to the knowledge repertoire of hybrid DNA condensates involving nanoparticles. The CD was found to generate ROS with visible light irradiation that could induce cytotoxicity issues. This should alert the researchers trying to establish them as potential transfection agents with the prospect of simultaneously tracking them after excitation with a relevant wavelength. Consequently, electrostatically held DNA on CD and the potential of the latter to generate ROS could endanger advanced downstream translational technology development of condensate-based nonviral vectors, where injectable formulations are delegated to carry the condensate cargo into targeted cells after spending a considerable amount of time in circulation if not microinjected at the site. Even though the CD-pUC19 condensates were found to enter HEK293 cells with ease and display bright blue fluorescence, this does not guarantee that the DNA that is covalently conjugated to CD is released in the nucleus or whether the DNA can insert itself into the nucleus, which calls for further examination. However, careful inspection of knowledge generated through our present study should provide the preamble to realize CDs as potential nonviral vectors whose future otherwise looks bright similar to their fluorescence.

EXPERIMENTAL SECTION

Materials. Citric acid monohydrate, cysteamine, 1-methylimidazole ($C_4H_6N_2$), EDC hydrochloride (EDC·HCl), methylthiazolyldiphenyl tetrazolium bromide (MTT), phosphate-buffered saline (PBS), and spermine were purchased from Sigma. pUC19 plasmid and HINDIII restriction endonuclease and supercoiled DNA ladder (1 kbp) were obtained from NEB. All chemicals were used as received. Nanopure water from Millipore was used in all experiments.

Instrumentation. PXRD analysis of the CD was done with Cu Kα (λ = 1.54 Å) X-ray source on a Rigaku TTRX-III instrument at a scanning rate of 2° per minute and a voltage of 10 kV in the 2θ range of 4−60°. FT-IR experiment was done on a PerkinElmer Spectrum-400 using KBr pellet within the range of 500−4000 cm^{-1}. UV−vis absorption spectra data were recorded on a UV-2550 spectrophotometer (Shimadzu, Japan). Steady-state fluorescence spectra were recorded on a Fluoromax-400 spectrofluorometer (Horiba, Japan). Time-resolved fluorescence decay was measured by a time-resolved fluorescence spectrophotometer from Edinburgh Instruments (LifeSpec-II, UK) working on the time-correlated single-photon counting technique. Circular dichroism spectroscopy was performed on a J-1500 spectropolarimeter (Jasco, UK).

https://doi.org/10.1021/acsomega.1c02247
ACS Omega 2021, 6, 21425−21435

Preparation of CDs. CDs were synthesized by the thermal decomposition method by dissolving cysteamine (8.7 mmol, 0.64 g) and citric acid (10 mmol, 2.10 g) in 10 mL of water.[21,22] The clear solution was transferred to a 50 mL beaker and heated at 200 °C on a hot plate for 2 h. The yellowish viscous solution obtained was diluted to 50 mL with water and centrifuged at 10,000 rpm to settle down the large particle and collect the supernatant. Then, the resultant solution was filtered through a 0.2 μm syringe filter to remove large aggregates. The samples were dialyzed (membrane MWCO = 1 kDa) against water for 2 days with occasional changing of water to eliminate the starting material and impurities.

Determination of Quantum Yield of CDs. For the determination of quantum yield, a solution of quinine sulfate (QY = 0.55) in 0.5 M H_2SO_4 was used as the standard.[35] The solutions of CD in water and quinine sulfate in H_2SO_4 were prepared to have similar absorbance at the excitation wavelength. Quantum yield was calculated by using the following equation

$$\Phi_x = \Phi_s \times (I_x f_s \eta_x^2 / I_s f_x \eta_s^2)$$

where subscript x and s denote the test and standard sample, respectively; Φ is the fluorescence quantum yield; I is the integrated fluorescence intensity; f is the absorption factor ($f = 1 - 10^{-A}$, where A = absorbance); and η is the refractive index of the solvent.

Linearization of pUC19 DNA by HindIII. Circular pUC19 plasmid was linearized with HindIII restriction endonuclease having a single restriction site. 1 μL of plasmid (1 μg/μL) was treated with 1 μL of HINDIII (10 U/μL) restriction endonuclease in the presence of 1× HindIII buffer in a total volume of 20 μL for 6 h at 37 °C. The linear plasmid sample was purified by ethanol precipitation, followed by washing with 80% ethanol (20% NaCl) and air-dried. The sample was equilibrated by the addition of PBS (10 mM sodium phosphate, 0.15 M NaCl, 10 mM EDTA, pH 7.2) to solubilize the linear plasmid for further downstream use. The linear plasmid sample was subjected to 1% agarose gel electrophoresis, stained with ethidium bromide solution, and destained to confirm the success of the restriction digestion. The concentration of the linear pUC19 was determined by measuring the absorbance at 260 nm in a UV−vis spectrophotometer.

Conjugation of the CD with Linearized pUC19. The 5′phosphate end of linearized pUC19 was conjugated with the aqueous soluble CD having surface amine functionality by EDC-imidazole coupling chemistry.[36] 1.25 mg (6.52 μM) of EDC was weighed in a microcentrifuge tube, followed by the addition of 10 μL of linearized pUC19 (10 nM) solution with continuous stirring until the contents were completely dissolved. 10 μL (0.1 M) of 1-methyl imidazole was added to the reaction mixture, and the transparent solution was further stirred at 37 °C for 2 h. To this solution, 10 μL of CD (5 mg/mL) was added with continuous stirring at 37 °C overnight, followed by dialysis of the sample to obtain the CD-pUC19 covalent conjugate. The concentration of the plasmid and CD present in the ensemble was determined by UV−vis spectroscopy.

Preparation of CD-pUC19 Condensates. DNA condensation was done under dust-free conditions after filtering the solutions with centrifugal filters (diameter 0.22 μm, Millipore). Condensation reactions were performed in 10 mM sodium phosphate buffer (pH 7.2). A solution of 10 μL of CD-pUC19 conjugated product (25 μg/mL DNA and 20 μg/mL CD) in sodium phosphate buffer was added slowly to an equal volume of spermine solutions (25−250 μM) to a total volume of 20 μL with a resultant plasmid concentration of 12.5 μg/mL and spermine concentration as exactly half as the initial concentration used. Following 5 min of gentle agitation, the DNA condensates were subjected to further analysis including gel electrophoresis and electron microscopy.

RP-HPLC Analysis. RP-HPLC was done on a Shimadzu Prominence analytical HPLC system (Shimadzu, Japan) that is connected with a controller (CBM-20Alite), pump (LC-20AD), and PDA detector (SPD-M20A) using a C18G (250 × 4.6 mm) column. Elution was done by an in-house-developed gradient profile particularly suitable to elute CD. The mobile phase contained (95:5)% of 10 mM Tris-HCl buffer (pH 7.4) as eluent A and acetonitrile as eluent B. The flow rate was 0.2 mL/min with 25 ± 1 °C column temperature and 10 μL injection volumes.

DLS and Measurement of Zeta Potential. For DLS study, a solution of CD-plasmid (25 μg/mL DNA and 20 μg/mL CDs) was added to an equal volume of spermine solutions (25−250 μM). All experiments were performed in 10 mM sodium phosphate buffer (pH 7.2). All solutions were filtered through a syringe filter (0.2 μm) before introducing them into the light scattering instrument. After ∼5 min of gentle agitation, the mean hydrodynamic diameter of the samples was measured using Nanoparticles Tracking Analysis (NTA, Nanosight NS300, Malvern Panalytical, UK) and analyzed by a single cumulative fit. The zeta potential was measured by using a Zetasizer (Nano Z, Malvern Panalytical, UK).

Fluorescence Titration Studies. Fluorescence intensity changes were monitored at the emission maximum of 420 nm upon excitation at 345 nm of different concentrations (25−400 μM) of spermine that were added to 100 μL of CD (20 μg/mL) or CD-pUC19 conjugate sample (25 μg/mL DNA and 20 μg/mL CD). Each measurement was executed after 2 min of spermine addition. The fluorescence titration data were used for the determination of binding constants with the modified Benesi−Hilderbrand equation.

$$\frac{1}{\Delta F} = \frac{1}{\Delta F_{max}} + \frac{1}{\Delta F_{max} K_b} \times \frac{1}{[\text{spermine}]}$$

where ΔF is the difference in the fluorescence intensity of the CD without and with different concentrations of spermine. ΔF_{max} is the difference between the maximum fluorescence intensity of the CD in the presence and absence of spermine. K_b is obtained from the intercept to the slope ratio of the double reciprocal linear plot.

Isothermal Titration Calorimetry. ITC measurements were performed in a MicroCal iTC200 (GE Healthcare) at 30 °C. 200 μL of pUC19 or CD-pUC19 (0.1 mM) solution was loaded in the sample cell as the substrate and 0.1 mM spermine solution was taken in the injection syringe. After the equilibration time of the calorimeter and an initial delay of 60 s, a substrate solution (2 μL) was injected 20 times consecutively with an interval of 120 s with a rotation speed of 750 rpm. The integrated area under each heat burst curve was calculated to find the heat associated with the injections. To measure the heat of dilution, a control experiment was also performed using spermine and buffer solution. The injecting heats were plotted as a function of the CD-pUC19/spermine

https://doi.org/10.1021/acsomega.1c02247
ACS Omega 2021, 6, 21425−21435

ratio and fitted with a model of one set of binding sites. The data were analyzed to obtain the binding affinity (K_a), the binding stoichiometry (N), and the enthalpy of binding (ΔH°). The binding Gibbs energy change (ΔG°) and the entropic contribution to the binding ($T\Delta S^\circ$) were calculated from the standard thermodynamic equations, such as $\Delta G^\circ = -RT \ln K_a$ and $\Delta G^\circ = \Delta H^\circ - T\Delta S^\circ$.

Microscopy Experiments. AFM images were obtained by casting a small volume of freshly prepared CD/CD-pUC19 condensate on an APS mica sheet. Images were captured in the intermittent noncontact mode AFM (ACAFM) using a Keysight 5500 scanning probe microscope. Commercial silicon nitride cantilevers having a force constant of 40 N/m were used for the measurements (Micromesh, Bulgaria). The cantilever was oscillating at its resonance frequency ranging from 265 to 410 kHz.

TEM analysis was done with a diluted sample (5 μL) applied on a carbon-coated copper TEM grid (Ted Pella). The excess sample was dried off by gently touching the edge with a piece of filter paper and then air-dried. Images of the CD-pUC19 condensate at room temperature were acquired by a JEM-F200 transmission electron microscope operated at 100 kV and 100,000× magnifications.

Study of the ROS Generation Efficiency. The ROS generation efficiencies of CD and CD-pUC19 condensate were studied in the presence of DHR 123. DHR 123 (5 μL, 1 nM) solution was added to the respective sample solutions and irradiated with a tungsten bulb (Philips, 100 W) at ∼30 cm distance.[20,21] The nonfluorescent DHR 123 was oxidized to fluorescent rhodamine 123 in the presence of ROS, generated from CD whose steady-state spectra were recorded in the wavelength range of 500−600 nm (480 nm excitation wavelength) at 10 min interval up to 60 min.

Cell Culture and Cell Imaging. HEK293 (human embryonic kidney 293) cells were cultured in Dulbecco's modified Eagle's medium (with 10% FBS), incubated in a CO_2 incubator at 37 °C in 5% CO_2, and passaged every 3 days by trypsinization. For confocal imaging, HEK293 cells were cultured on coverslips in a 24-well plate at the density of 30,000 cells/well. The medium was removed after 24 h, and cells were washed with PBS. The CD and CD-PUC19 condensate (1 μg/mL) were then added to the respective well and incubated for 2 h, followed by repeated washing with PBS, fixed with 4% PFA for 20 min, followed by PBS wash, and mounted on slides. A Nikon-TiE confocal microscope was used for imaging the cells..

■ ASSOCIATED CONTENT

Supporting Information

The Supporting Information is available free of charge at https://pubs.acs.org/doi/10.1021/acsomega.1c02247.

Experimental section, EDS analysis, HRTEM image, SAED pattern, FT-IR spectra, UV−vis spectra, steady-state spectra, agarose gel of CD-pUC19 with ladder, zeta potential of CD and linear pUC19, DLS of CD-pUC19 conjugate at 50 and 200 μM spermine, ITC of CD and linear pUC19 with spermine, fluorescence titration of CD with spermine, ITC data of binding, fluorescence lifetime data, TEM images of condensates, RO generation by CD, gel electrophoresis for decondensation, MTT assay, and confocal images of transfection efficiency (PDF)

■ AUTHOR INFORMATION

Corresponding Author

Prolay Das − *Department of Chemistry, Indian Institute of Technology Patna, Bihta 801106 Bihar, India;* orcid.org/0000-0002-2774-8479; Email: prolay@iitp.ac.in

Author

Suman Nayak − *Department of Chemistry, Indian Institute of Technology Patna, Bihta 801106 Bihar, India*

Complete contact information is available at: https://pubs.acs.org/10.1021/acsomega.1c02247

Author Contributions

S.N.—methodology, data curation, investigation, visualization, and writing—original draft. P.D.—conceptualization, validation, supervision, and writing—review and editing. The manuscript was written through the contributions of all authors. All authors have given approval to the final version of the manuscript.

Notes

The authors declare no competing financial interest.

■ ACKNOWLEDGMENTS

The authors thank IIT Patna for infrastructure, funding, and experimental facilities. S.N. is thankful to IIT Patna for fellowship.

■ REFERENCES

(1) Unnikrishnan, B.; Wu, R.-S.; Wei, S.-C.; Huang, C.-C.; Chang, H.-T. Fluorescent Carbon Dots for Selective Labeling of Subcellular Organelles. *ACS Omega* **2020**, *5*, 11248−11261.

(2) Anwar, S.; Ding, H.; Xu, M.; Hu, X.; Li, Z.; Wang, J.; Liu, L.; Jiang, L.; Wang, D.; Dong, C.; Yan, M.; Wang, Q.; Bi, H. Recent advances in synthesis, optical properties, and biomedical applications of carbon dots. *ACS Appl. Bio Mater.* **2019**, *2*, 2317−2338.

(3) Molaei, M. J. Carbon quantum dots and their biomedical and therapeutic applications: a review. *RSC Adv.* **2019**, *9*, 6460−6481.

(4) Liu, C.; Zhang, P.; Zhai, X.; Tian, F.; Li, W.; Yang, J.; Liu, Y.; Wang, H.; Wang, W.; Liu, W. Nano-carrier for gene delivery and bioimaging based on carbon dots with PEI-passivation enhanced fluorescence. *Biomaterials* **2012**, *33*, 3604−3613.

(5) Cao, X.; Wang, J.; Deng, W.; Chen, J.; Wang, Y.; Zhou, J.; Du, P.; Xu, W.; Wang, Q.; Wang, Q.; Yu, Q. Photoluminescent cationic carbon dots as efficient non-viral delivery of plasmid SOX9 and chondrogenesis of fibroblasts. *Sci. Rep.* **2018**, *8*, 7057.

(6) He, X.; Chen, P.; Zhang, J.; Luo, T.-Y.; Wang, H.-J.; Liu, Y.-H.; Yu, X.-Q. Cationic polymer-derived carbon dots for enhanced gene delivery and cell imaging. *Biomater. Sci.* **2019**, *7*, 1940−1948.

(7) Zhou, J.; Deng, W.; Wang, Y.; Cao, X.; Chen, J.; Wang, Q.; Xu, W.; Du, P.; Yu, Q.; Chen, J.; Spector, M.; Yu, J.; Xu, X. Cationic carbon quantum dots derived from alginate for gene delivery: one-step synthesis and cellular uptake. *Acta Biomater.* **2016**, *42*, 209−219.

(8) Zuo, G.; Xie, A.; Pan, X.; Su, T.; Li, J.; Dong, W. Fluorine-doped cationic carbon dots for efficient gene delivery. *ACS Appl. Nano Mater.* **2018**, *1*, 2376−2385.

(9) Cui, H.; Xia, J.; Zhang, L.; Qian, M.; Wang, H.; Wang, J.; Chen, Q. Integument of Cytoplasmic Membrane onto Cationic DNA Condensates for Selective Gene Expression at Homologous Cells. *ACS Appl. Bio Mater.* **2019**, *2*, 4537−4544.

(10) Zhang, M.; Zhao, X.; Fang, Z.; Niu, Y.; Lou, J.; Wu, Y.; Zou, S.; Xia, S.; Sun, M.; Du, F. Fabrication of HA/PEI-functionalized carbon dots for tumor targeting, intracellular imaging and gene delivery. *RSC Adv.* **2017**, *7*, 3369−3375.

(11) Mohammadinejad, R.; Dadashzadeh, A.; Moghassemi, S.; Ashrafizadeh, M.; Dehshahri, A.; Pardakhty, A.; Sassan, H.; Sohrevardi, S.-M.; Mandegary, A. Shedding light on gene therapy:

Carbon dots for the minimally invasive image-guided delivery of plasmids and noncoding RNAs-A review. *J. Adv. Res.* **2019**, *18*, 81−93.
(12) Li, G.-Y.; Guan, R.-L.; Ji, L.-N.; Chao, H. DNA condensation induced by metal complexes. *Coord. Chem. Rev.* **2014**, *281*, 100−113.
(13) Bloomfield, V. A. DNA condensation by multivalent cations. *Biopolymers* **1997**, *44*, 269−282.
(14) Cheng, L.; Li, Y.; Zhai, X.; Xu, B.; Cao, Z.; Liu, W. Polycation-b-polyzwitterion copolymer grafted luminescent carbon dots as a multifunctional platform for serum-resistant gene delivery and bioimaging. *ACS Appl. Mater. Interfaces* **2014**, *6*, 20487−20497.
(15) Pierrat, P.; Wang, R.; Kereselidze, D.; Lux, M.; Didier, P.; Kichler, A.; Pons, F.; Lebeau, L. Efficient in vitro and in vivo pulmonary delivery of nucleic acid by carbon dot-based nanocarriers. *Biomaterials* **2015**, *51*, 290−302.
(16) Dou, Q.; Jiang, S.; Fang, X. Multi-functional fluorescent carbon dots with antibacterial and gene delivery properties. *RSC Adv.* **2015**, *5*, 46817−46822.
(17) Chen, J.; Wang, Q.; Zhou, J.; Deng, W.; Yu, Q.; Cao, X.; Wang, J.; Shao, F.; Li, Y.; Ma, P.; Spector, M.; Yu, J.; Xu, X. Porphyra polysaccharide-derived carbon dots for non-viral co-delivery of different gene combinations and neuronal differentiation of ectodermal mesenchymal stem cells. *Nanoscale* **2017**, *9*, 10820−10831.
(18) Porschke, D. Dynamics of DNA condensation. *Biochemistry* **1984**, *23*, 4821−4828.
(19) Matulis, D.; Rouzina, I.; Bloomfield, V. A. Thermodynamics of DNA binding and condensation: isothermal titration calorimetry and electrostatic mechanism. *J. Mol. Biol.* **2000**, *296*, 1053−1063.
(20) Mandal, S.; Prasad, S. R.; Mandal, D.; Das, P. Bovine Serum Albumin Amplified Reactive Oxygen Species Generation from Anthrarufin-Derived Carbon Dot and Concomitant Nanoassembly for Combination Antibiotic−Photodynamic Therapy Application. *ACS Appl. Mater. Interfaces* **2019**, *11*, 33273−33284.
(21) Nayak, S.; Prasad, S. R.; Mandal, D.; Das, P. Hybrid DNA−Carbon Dot−Poly (vinylpyrrolidone) Hydrogel with Self-Healing and Shape Memory Properties for Simultaneous Trackable Drug Delivery and Visible-Light-Induced Antimicrobial Photodynamic Inactivation. *ACS Appl. Bio Mater.* **2020**, *3*, 7865−7875.
(22) Nayak, S.; Prasad, S. R.; Mandal, D.; Das, P. Carbon dot cross-linked polyvinylpyrrolidone hybrid hydrogel for simultaneous dye adsorption, photodegradation and bacterial elimination from waste water. *J. Hazard. Mater.* **2020**, *392*, 122287.
(23) Sharma, A.; Das, J. Small molecules derived carbon dots: synthesis and applications in sensing, catalysis, imaging, and biomedicine. *J. Nanobiotechnol.* **2019**, *17*, 92.
(24) Yang, W.; Zhang, H.; Lai, J.; Peng, X.; Hu, Y.; Gu, W.; Ye, L. Carbon dots with red-shifted photoluminescence by fluorine doping for optical bio-imaging. *Carbon* **2018**, *128*, 78−85.
(25) Das, P.; Schuster, G. B. Effect of condensate formation on long-distance radical cation migration in DNA. *Proc. Natl. Acad. Sci.* **2005**, *102*, 14227−14231.
(26) Das, P.; Schuster, G. B. One-electron oxidation of condensed DNA toroids: Injection-site dependent charge (radical cation) mobility. *Bioconjugate Chem.* **2008**, *19*, 1235−1240.
(27) Singh, V.; Das, P. Condensation of DNA—A putative obstruction for repair process in abasic clustered DNA damage. *DNA Repair* **2013**, *12*, 450−457.
(28) Lin, Z.; Wang, C.; Feng, X.; Liu, M.; Li, J.; Bai, C. The observation of the local ordering characteristics of spermidine-condensed DNA: atomic force microscopy and polarizing microscopy studies. *Nucleic Acids Res.* **1998**, *26*, 3228−3234.
(29) Pramanik, S.; Chatterjee, S.; Suresh Kumar, G.; Sujatha Devi, P. Egg-shell derived carbon dots for base pair selective DNA binding and recognition. *Phys. Chem. Chem. Phys.* **2018**, *20*, 20476−20488.
(30) Gupta, S.; Tiwari, N.; Munde, M. A comprehensive biophysical analysis of the effect of DNA binding drugs on protamine-induced DNA condensation. *Sci. Rep.* **2019**, *9*, 5891.
(31) Patel, M. M.; Anchordoquy, T. J. Contribution of hydrophobicity to thermodynamics of ligand-DNA binding and DNA collapse. *Biophys. J.* **2005**, *88*, 2089−2103.
(32) Vijayanathan, V.; Agostinelli, E.; Thomas, T.; Thomas, T. J. Innovative approaches to the use of polyamines for DNA nanoparticle preparation for gene therapy. *Amino Acids* **2014**, *46*, 499−509.
(33) Chang, Y.-M.; Chen, C. K.-M.; Hou, M.-H. Conformational changes in DNA upon ligand binding monitored by circular dichroism. *Int. J. Mol. Sci.* **2012**, *13*, 3394−3413.
(34) Barman, M. K.; Patra, A. Current status and prospects on chemical structure driven photoluminescence behaviour of carbon dots. *J. Photochem. Photobiol., C* **2018**, *37*, 1−22.
(35) Pandit, S.; Behera, P.; Sahoo, J.; De, M. In situ synthesis of amino acid functionalized carbon dots with tunable properties and their biological applications. *ACS Appl. Bio Mater.* **2019**, *2*, 3393−3403.
(36) Kumari, S.; Rajit Prasad, S.; Mandal, D.; Das, P. Carbon dot-DNA-protoporphyrin hybrid hydrogel for sustained photoinduced antimicrobial activity. *J. Colloid Interface Sci.* **2019**, *553*, 228−238.

https://doi.org/10.1021/acsomega.1c02247
ACS Omega 2021, 6, 21425−21435